Available online at www.sciencedirect.com
SCIENCE DIRECT®
Journal of Power Sources 130 (2004) 149–157
JOURNAL OF POWER SOURCES
www.elsevier.com/locate/jpowsour

Computational model of a PEM fuel cell with serpentine gas flow channels

Phong Thanh Nguyen, Torsten Berning[1], Ned Djilali*

Institute for Integrated Energy Systems, University of Victoria, Victoria, Canada BC V8W 3P6

Received 25 September 2003; accepted 3 December 2003

Abstract

A three-dimensional computational fluid dynamics model of a PEM fuel cell with serpentine flow field channels is presented in this paper. This comprehensive model accounts for the major transport phenomena in a PEM fuel cell: convective and diffusive heat and mass transfer, electrode kinetics, and potential fields. A unique feature of the model is the implementation of a voltage-to-current (VTC) algorithm that solves for the potential fields and allows for the computation of the local activation overpotential. The coupling of the local activation overpotential distribution and reactant concentration makes it possible to predict the local current density distribution more accurately. The simulation results reveal current distribution patterns that are significantly different from those obtained in studies assuming constant surface overpotential. Whereas the predicted distributions at high load show current density maxima under the gas channel area, low load simulations exhibit local current maxima under the collector plate land areas.

Keywords: PEM fuel cells; Fuel cell modeling; Overpotential; Simulation; CFD

1. Introduction

Because of the highly reactive environment of a fuel cell it is not possible to perform detailed in situ measurements during operation. Yet such detailed information is required in order to improve understanding of water and species transport and of thermal effects. Modeling and simulation tools that can provide such information and predict the effect of various operating and material parameters would contribute to significantly shorter design and optimization cycles. The development of comprehensive and reliable computational models is a challenging task because the processes involve multi-component, multi-phase, and multi-dimensional flow, heat and mass transfer with electro-chemical reactions; all occurring in irregular geometries including porous media. Extensive research efforts have been devoted to develop realistic simulation models in the past decade. The first two models were published in the early 1990s by Springer et al. [1] and Bernardi and Verbrugge [2]. These models are one-dimensional and only account for diffusive mass transport and electrochemical kinetics. From 1993 to 1998, several two-dimensional models were published by Nguyen and White [3], Fuller and Newman [4], and Gurau et al. [5]. Most of these assume some concentration profile of reactant species along the channel except for Gurau's model, which accounts directly for convective mass transport.

The application of CFD methodology to fuel cell modeling has spurred significant progress including three-dimensional capabilities [6] and two-phase transport [7–9]. In order to simplify the numerical procedure and make the problems computationally tractable, multi-dimensional CFD models have relied on the linearization of the Butler–Volmer equation by assuming a constant surface overpotential. In addition, most fuel cell models presented to date use straight gas flow channel configurations, whereas serpentine flow channels are commonly used in many fuel cell flow plate design.

This paper presents a three-dimensional model with serpentine gas flow channels. The model accounts for detailed species mass transport, heat transfer, potential losses in the gas diffusion layers (GDL) and membrane, and electrochemical kinetics. In addition to the complex geometry, the model features an algorithm that allows for a more realistic representation of the local activation overpotentials which

* Corresponding author. Tel.: +1-250-7216034; fax: +1-250-7216051.
E-mail address: ndjilali@uvic.ca (N. Djilali).
[1] Currently at the Institute for Material Technology, Group of Electrochemistry, NTNU Trondheim, Norway.

0378-7753/$ – see front matter © 2004 Elsevier B.V. All rights reserved.
doi:10.1016/j.jpowsour.2003.12.027

Nomenclature

A_{MEA}	area of the MEA (cm^2)
A_{Ch}	cross sectional area of flow channel (cm^2)
a	active surface per unit volume ($cm^2\,cm^{-3}$)
C_{H_2}	local hydrogen concentration ($mol\,m^{-3}$)
$C_{H_2}^{ref}$	reference hydrogen concentration ($mol\,m^{-3}$)
C_{O_2}	local oxygen concentration ($mol\,m^{-3}$)
$C_{O_2}^{ref}$	reference oxygen concentration ($mol\,m^{-3}$)
C_p	specific heat capacity ($J\,kg^{-1}\,K^{-1}$)
D	diffusion coefficients ($m^2\,s^{-1}$)
E_{cell}	cell operating potential (V)
E_{rev}	reversible cell potential (V)
F	Faraday's constant 96487 ($C\,mol^{-1}$)
h	total specific enthalpy ($J\,kg^{-1}$)
I	cell operating current density ($A\,cm^{-2}$)
i_a	anode volumetric current density ($A\,cm^{-3}$)
i_c	cathode volumetric current density ($A\,cm^{-3}$)
$i_{o,a}^{ref}$	anode reference exchange current density ($A\,cm^{-3}$)
$i_{o,c}^{ref}$	cathode reference exchange current density ($A\,m^{-3}$)
k_p	hydraulic permeability (m^2)
L	channel length (m)
M_{O_2}	molecular weight of oxygen ($kg\,mol^{-1}$)
M_{H_2}	molecular weight of hydrogen ($kg\,mol^{-1}$)
M_{H_2O}	molecular weight of water ($kg\,mol^{-1}$)
N_w	net water flux across the membrane ($kg\,m^{-2}\,s^{-1}$)
n_e	number of electrons transfered
p	pressure (Pa)
$\dot{q}$	heat generation ($W\,m^{-3}$)
R	universal gas constant ($8.314\,J\,mol^{-1}\,K^{-1}$)
s	specific entropy ($J\,mol^{-1}\,K^{-1}$)
T	temperature (K)
$\mathbf{u}$	velocity vector ($m\,s^{-1}$)
x_i	molar fraction
Y_i	mass fraction
α	charge transfer coefficient
ε	porosity
γ	concentration parameter
η	overpotential (V)
λ_{eff}	effective electrode thermal conductivity ($W\,m^{-1}\,K^{-1}$)
λ_{gr}	thermal conductivity of graphite ($W\,m^{-1}\,K^{-1}$)
λ_e	electrode electronic conductivity ($S\,m^{-1}$)
λ_m	membrane protonic conductivity ($S\,m^{-1}$)
μ	viscosity ($kg\,m^{-1}\,s^{-1}$)
ρ	density ($kg\,m^{-3}$)
ξ	stoichiometric flow ratio

leads to improved prediction of the local current density distribution.

2. Model development

2.1. Model assumptions

In common with many detailed three-dimensional models, steady state operation under fully humidified conditions is assumed. While transients are encountered in practice, this is beyond the scope of this work. The model is also restricted to single-phase water transport in the gas diffusion electrodes and gas flow channels and assumes operation under ideal heat and water management ensuring the membrane remains fully humidified. Issues related to two-phase transport and water condensation are discussed in Ref. [9].

Both humidified air and hydrogen behave as ideal gases and since the characteristic Reynolds number in the gas channels are low the flows there are assumed laminar.

Other assumptions used in the model are as follows:

- Anode and cathode gases are not permitted to crossover, i.e. the membrane is impermeable.
- Ohmic heating is neglected as heat generation is assumed to be predominantly associated with the cathodic electrochemical reaction [10].
- Water is assumed to exist in the vapor phase, only consistent with the assumption of single-phase water transport.
- The potential drop in the bipolar plate is negligible since graphite is a good conductor.

2.2. Computational domain

A computational model of an entire cell would require very large computing resources and excessively long simulation times. The computational domain in this study is therefore limited to one turn of a serpentine channel as shown Fig. 1.

2.3. Governing equations

The governing Eqs. corresponding to the various regions of the fuel cell are given below.

The flow in the reactant gas channels is governed by the Navier–Stokes equation.

Continuity equation:

$$\nabla \cdot (\rho \mathbf{u}) = 0 \tag{1}$$

Momentum equation:

$$\nabla \cdot (\rho \mathbf{u} \otimes \mathbf{u} - \mu \nabla \mathbf{u}) = -\nabla (p + \tfrac{2}{3}\mu \nabla \cdot \mathbf{u}) + \nabla \cdot [\mu (\nabla \mathbf{u})^{\mathrm{T}}] \tag{2}$$

Energy equation:

$$\nabla \cdot (\rho \mathbf{u} h) - \nabla \cdot (k \nabla T) = 0 \tag{3}$$

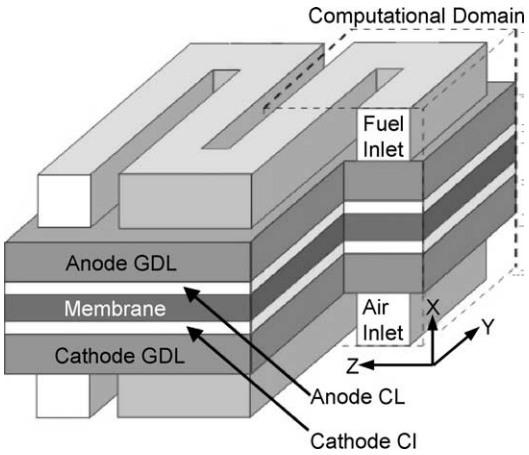

Fig. 1. Geometry of serpentine flow channel fuel cell and boundaries of the computational domain. (GDL is gas diffusion electrode; CL is the catalyst layer).

Mass transport:

$$\nabla \cdot (\rho \mathbf{u} Y_i) - \nabla \cdot (\rho D_{(ii)} \nabla Y_i) = \nabla \cdot (\rho D_{(ij)} \nabla Y_j) \quad (4)$$

where the subscript i denotes oxygen at the cathode side and hydrogen at the anode side, and j is water vapor in both cases. The diffusion coefficients $D_{(ii)}$ and $D_{(ij)}$ are Stefan–Maxwell ternary diffusion coefficients and are obtained following Taylor and Krishna [11]. The gas mixture is assumed well mixed at the molecular level, with all components sharing the same velocity, pressure, and temperature fields.

Transport in the gas diffusion layer is modeled as transport in a porous media. The continuity equation in the gas diffusion layers becomes:

$$\nabla \cdot (\rho \varepsilon \mathbf{u}) = 0 \quad (5)$$

The momentum equation reduces to Darcy's law

$$\mathbf{u} = -\frac{k_p}{\mu} \nabla p \quad (6)$$

and the mass transport equation in the GDL becomes

$$\nabla \cdot (\rho \varepsilon \mathbf{u} Y_i) - \nabla \cdot (\rho \varepsilon D_{ii} \nabla Y_i) = \nabla \cdot (\rho \varepsilon D_{ij} \nabla Y_j) \quad (7)$$

In order to account for geometric constraints of the porous media, the diffusivities are corrected using the Bruggemann correction formula

$$D_{ij}^{\text{eff}} = D_{ij} \times \varepsilon^{1.5} \quad (8)$$

The exponent of 1.5 was determined empirically [12]. It should be noted that the Bruggemann correction and the alternative correction based on tortuosity are essentially equivalent for low tortuosities and porosities in the range 0.4–0.5.

Heat transfer in the in the gas diffusion layers is governed by,

$$\nabla \cdot (\rho \varepsilon \mathbf{u} h) - \nabla \cdot (k_{\text{eff}} \varepsilon \nabla T) = \varepsilon S_q \quad (9)$$

where S_q is the source term for heat exchange to and from the solid matrix of the porous media.

The balance between the electro-osmotic drag of water (from anode to cathode) and back diffusion (from cathode to anode) yields the net water flux through the membrane

$$N_w = n_d M_{H_2O} \frac{i}{F} - \nabla \cdot (\rho D_w \nabla Y_w) \quad (10)$$

where n_d is the electro-osmotic drag coefficient and D_w is the water diffusion coefficient in the membrane.

The bipolar plates conduct heat and current. Electron conduction is assumed to be very fast in graphite and is not modeled here. Heat conduction in the bipolar plates is governed by

$$\nabla \cdot (k_{gr} \nabla T) = 0 \quad (11)$$

The potential distribution in the gas diffusion layers is governed by

$$\nabla \cdot (\lambda_e \nabla V) = S_e \quad (12)$$

Potential loss in the membrane is due to resistance to proton transport across the membrane, and is governed by a similar equation,

$$\nabla \cdot (\lambda_m \nabla V) = S_m \quad (13)$$

2.4. Electrochemical reaction kinetics

The consumption of reactant species and the production of water and heat are modeled as sink and source terms in the catalyst layers. The mass consumption rate of oxygen per unit volume is given by:

$$S_{O_2} = -\frac{M_{O_2}}{4F} i_c \quad (14)$$

The production of water is modeled as a source term based on the local current density,

$$S_{H_2O} = \frac{M_{H_2O}}{2F} i_c \quad (15)$$

At the anode catalyst layer, hydrogen is consumed to produce electrons and protons. The consumption of hydrogen is given by

$$S_{H_2} = -\frac{M_{H_2}}{2F} i_a \quad (16)$$

In this model, heat generation is assumed to be predominantly due to the electrochemical reactions, and ohmic heating is not currently accounted for. Furthermore, Lampinen and Fomino [10] showed that heat generation from the anode reaction is negligible compared to the cathode reaction, and hence only cathodic heat generation is considered:

$$\dot{q} = \left[\frac{T(-\Delta s)}{n_e F} + \eta_{act} \right] i_c \quad (17)$$

where T is the local temperature, Δs is the entropy of the chemical reaction, n_e is the number of electrons transferred per mole of hydrogen, η_{act} is the activation overpotential.

The local current density distribution in the catalyst layers is modeled by the Butler–Volmer equation.

$$i_c = i_{\mathrm{o,c}}^{\mathrm{ref}} \left(\frac{C_{\mathrm{O_2}}}{C_{\mathrm{O_2}}^{\mathrm{ref}}}\right)^{\gamma_{\mathrm{O_2}}} \left[\exp\left(\frac{\alpha_{\mathrm{a}} F}{RT}\eta_{\mathrm{act,c}}\right) - \exp\left(-\frac{\alpha_{\mathrm{c}} F}{RT}\eta_{\mathrm{act,c}}\right)\right] \quad (18)$$

$$i_{\mathrm{a}} = i_{\mathrm{o,a}}^{\mathrm{ref}} \left(\frac{C_{\mathrm{H_2}}}{C_{\mathrm{H_2}}^{\mathrm{ref}}}\right)^{\gamma_{\mathrm{H_2}}} \left[\exp\left(\frac{\alpha_{\mathrm{a}} F}{RT}\eta_{\mathrm{act,a}}\right) - \exp\left(-\frac{\alpha_{\mathrm{c}} F}{RT}\eta_{\mathrm{act,a}}\right)\right] \quad (19)$$

where $i_{\mathrm{o,c}}^{\mathrm{ref}}$ and $i_{\mathrm{o,a}}^{\mathrm{ref}}$ are the cathode reference exchange current density; α_{a} and α_{c} are the cathode anodic and cathodic charge transfer coefficients respectively; and γ is an empirical concentration parameter. The values of the electrochemical transport parameters are taken from [13] and are listed in Table 1. The variation of the exchange current density with temperature was computed using the empirical relation given by Parthasarathy et al. [14].

Given an input cell potential E_{cell}, the local cathode activation overpotential is calculated from

$$\eta_{\mathrm{act,c}} = E_{\mathrm{rev}} - E_{\mathrm{cell}} - \eta_{\mathrm{ohmic,gdl}} - \eta_{\mathrm{protonic,mem}} - \eta_{\mathrm{act,a}} \quad (20)$$

where E_{rev} is obtained from the Nernst equation

$$E_{\mathrm{rev}} = E^0 - \frac{RT}{2F}\ln\left(\frac{a_{\mathrm{H_2O}}}{a_{\mathrm{H_2}} a_{\mathrm{O_2}}^{1/2}}\right) \quad (21)$$

The ohmic and protonic overpotentials in Eq. (20) are calculated from the potential Eqs. (12) and (13) using

$$\eta_{\mathrm{ohmic}} = V_{\mathrm{CL}} - V_{\mathrm{ref}} \quad (22)$$

$$\eta_{\mathrm{ohmic}} = V_{\mathrm{CL,c}} - V_{\mathrm{CL,a}} \quad (23)$$

where V_{CL} is the potential at the catalyst layer and V_{ref} is the reference potential taken at the interface between the gas diffusion layer and the bipolar plate.

The anode activation overpotential is small and assumed to be uniform. It is calculated from a conditional loop. An initial guess of the anode activation overpotential is obtained from the average local current density at the anode side, i_{a} using the Butler–Volmer equation (Eq. (19)). An updated value of the anode activation is then computed based on the charge conservation condition

$$I_{\mathrm{total}} = \sum_{j=1}^{N_{\mathrm{c}}} i_{\mathrm{c},j} \times V_j = \sum_{j=1}^{N_{\mathrm{a}}} i_{\mathrm{a},j} \times V_j \quad (24)$$

where N_{c} and N_{a} are the total number of computational cells in the cathode and anode catalyst layers respectively; V_j is the computational cell volume.

It should be noted that in many previous studies the current is prescribed and a constant surface overpotential is assumed in order to linearize the Butler–Volmer equation.

Table 1
Model parameters

Parameter	Symbol	Value
Channel length (mm)	L	50
Channel width (mm)	w	1
Channel height (mm)	h	1
Land area width (mm)	w_{l}	1
Gas diffusion layer thickness (μm)	t_{gdl}	260
Wet membrane thickness (Nafion 117) (μm)	t_{mem}	230
Catalyst layer thickness (μm)	t_{cl}	28
Membrane porosity	ε	0.28
Electrode porosity	ε	0.4
Membrane ionic conductivity (humidified Nafion® 117) ($\mathrm{S\,m^{-1}}$)	λ_{m}	17
Electrode electronic conductivity (estimate) ($\mathrm{S\,m^{-1}}$)	λ_{e}	570
Cathodic charge transfer coefficient for cathode reaction	$\alpha_{\mathrm{c,c}}$	2
Anodic charge transfer coefficient for cathode reaction	$\alpha_{\mathrm{a,c}}$	2
Cathodic charge transfer coefficient for anode reaction	$\alpha_{\mathrm{c,a}}$	1
Anodic charge transfer coefficient for anode reaction	$\alpha_{\mathrm{a,a}}$	1
Hydrogen reference concentration ($\mathrm{mol\,cm^{-3}}$)	$C_{\mathrm{H_2}}^{\mathrm{ref}}$	5.64 E−5
Oxygen reference concentration ($\mathrm{mol\,cm^{-3}}$)	$C_{\mathrm{O_2}}^{\mathrm{ref}}$	3.39 E−6
Oxygen concentration parameter	$\gamma_{\mathrm{O_2}}$	0.5
Hydrogen concentration parameter	$\gamma_{\mathrm{H_2}}$	0.25
Cathode reference exchange current density ($\mathrm{A\,cm^{-3}}$)	$i_{\mathrm{o,c}}^{\mathrm{ref}}$	1.0 E−5
Anode reference exchange current density ($\mathrm{A\,cm^{-3}}$)	$i_{\mathrm{o,a}}^{\mathrm{ref}}$	1.4 E5
Membrane thermal conductivity ($\mathrm{W\,m^{-1}\,K^{-1}}$)	k_{m}	0.455
Electrode thermal conductivity (Ballard AvCarb®-P150) ($\mathrm{W\,m^{-1}\,K^{-1}}$)	k_{eff}	1.3
Membrane hydraulic permeability ($\mathrm{m^2}$)	k_{p}	1.8 E−18
Electrode hydraulic permeability ($\mathrm{m^2}$)	k_{p}	4.73 E−19

Table 2
Base case operating conditions

Parameter	Symbol	Value
Anode pressure	P_a	3 atm
Cathode pressure	P_c	3 atm
Cell temperature	T	353 K
Relative humidity of inlet fuel	φ_a	100%
Relative humidity of inlet air	φ_c	100%
Air stoichiometric ratio	ξ_c	2
Fuel stoichiometric ratio	ξ_a	2

In this work, the local activation overpotential distribution is calculated by using the iterative Voltage-to-Current algorithm described in Section 3.

2.5. Boundary conditions

The inlet velocities of air and fuel are calculated based on the cell current and stoichiometric flow ratio as follow,

$$U_{\text{inlet}} = \frac{\xi I}{n_e F} \frac{A_{\text{MEA}}}{A_{\text{Ch}}} \frac{RT}{x_i P_i} \tag{25}$$

where n_e equals 2 for the anode flow side and 4 for the cathode side.

Pressure boundary conditions are prescribed at the outlets to simulate the operating pressure of the fuel cell. Symmetry boundary conditions are applied in the x–y plane of the computational domain. Zero heat flux is applied at the x–z plane of the conducting boundary surfaces.

A combination of Dirichlet and Neumann boundary conditions are used to solve the electronic and protonic potential equations. A reference potential is applied at the interface between the GDLs and the bipolar plate (land area).

The geometric and physico-chemical parameters are listed in Table 1, and the base case operating conditions in Table 2.

3. Solution algorithm

The governing equations and appropriate boundary conditions were implemented and solved using a 3 D commercial Computational Fluid Dynamics package (CFX-4.3) that employs a finite volume formulation. The discretized sets of algebraic equations are solved using the full field Stone's method for the momentum and scalar transport equations, and an algebraic multi-grid method for the pressure and energy equations. The properties are updated after each global iterative loop based on the new local gas composition and temperature using the relations given in Ref. [6].

The computational mesh consisted of a body-fitted grid with 351000 computational cells. The Fortran user subroutines developed previously [6] to solve the electrochemical component of the model were adapted and a new VTC algorithm was implemented.

A unique feature of the iterative VTC algorithm developed in this work is its capability for accurate calculation of the local activation overpotentials, which in turn results in improved prediction of the current density distribution. This algorithm is capable of predicting the cell current density based on a target cell operating voltage. The flowchart for the algorithm is shown in Fig. 2.

The improved predictive capabilities of the iterative VTC algorithm come with the penalty of higher computational

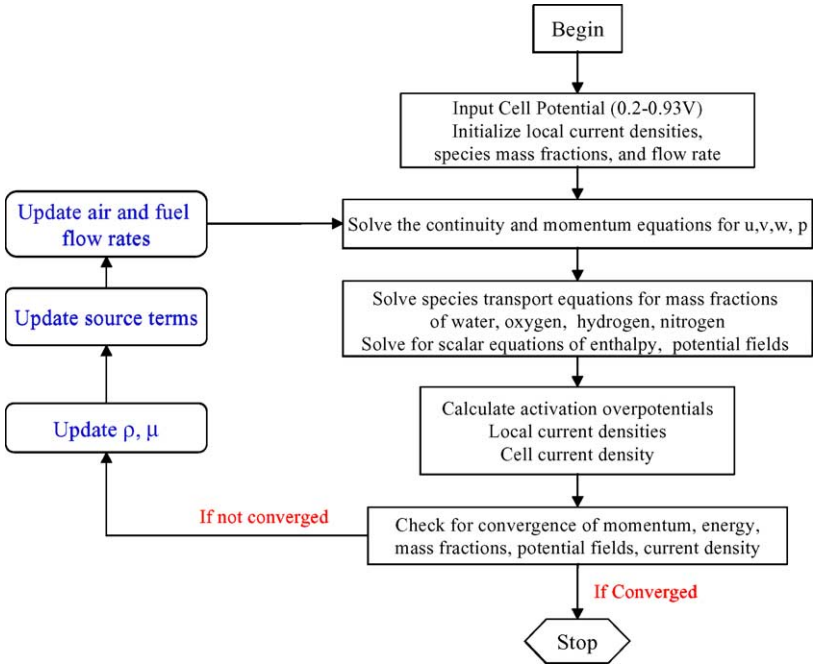

Fig. 2. Voltage-to-current (VTC) algorithm.

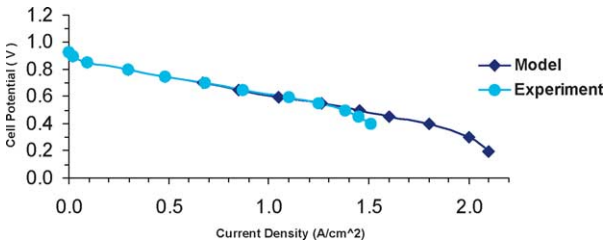

Fig. 3. Comparison of model and experimental polarization curves.

costs. Depending on the prescribed operating voltage, simulations with the VTC algorithm require about 6000–8000 iterations to achieve convergence; the higher the load the slower the convergence.

4. Results and discussions

The simulation results for base case operating conditions were verified against measurements of Ref. [15] obtained for the same conditions (Table 2). The computed polarization curve shown in Fig. 3 is in good agreement with the experimental polarization curve in the low load region. However, the model cell current densities in the mass transport limited region (>1.25 A cm^{-2}) are higher than the experimental values. This discrepancy is a common feature of single-phase models where the effect of reduced oxygen transport due to water flooding at the cathode at high current density [9] cannot be accounted for. In addition to this flooding effect, anode drying can also be a contributing factor to the reduced performance at high current density.

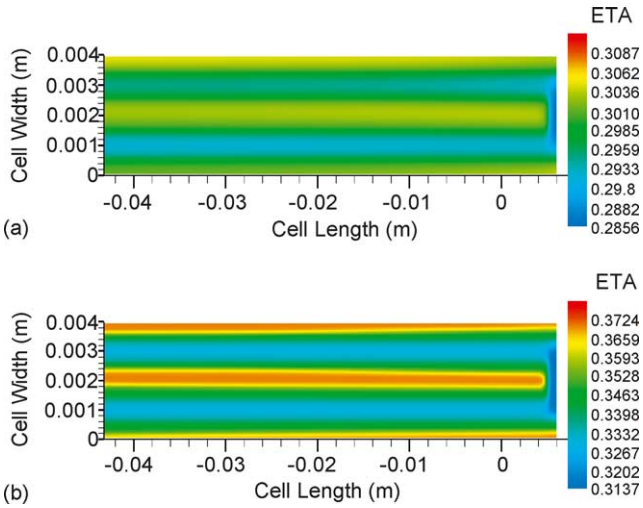

Fig. 5. Activation overpotential (in volts) distribution in the first catalyst layer for two loading conditions: (a) 0.3 A cm^{-2} and (b) 1.2 A cm^{-2}.

The detailed distribution of oxygen mass fractions for two different loading conditions is shown in Fig. 4. Oxygen concentration decreases from the inflow channel to the outflow channel. In the GDL, oxygen concentration under the land area is smaller than that under the channel area. This effect

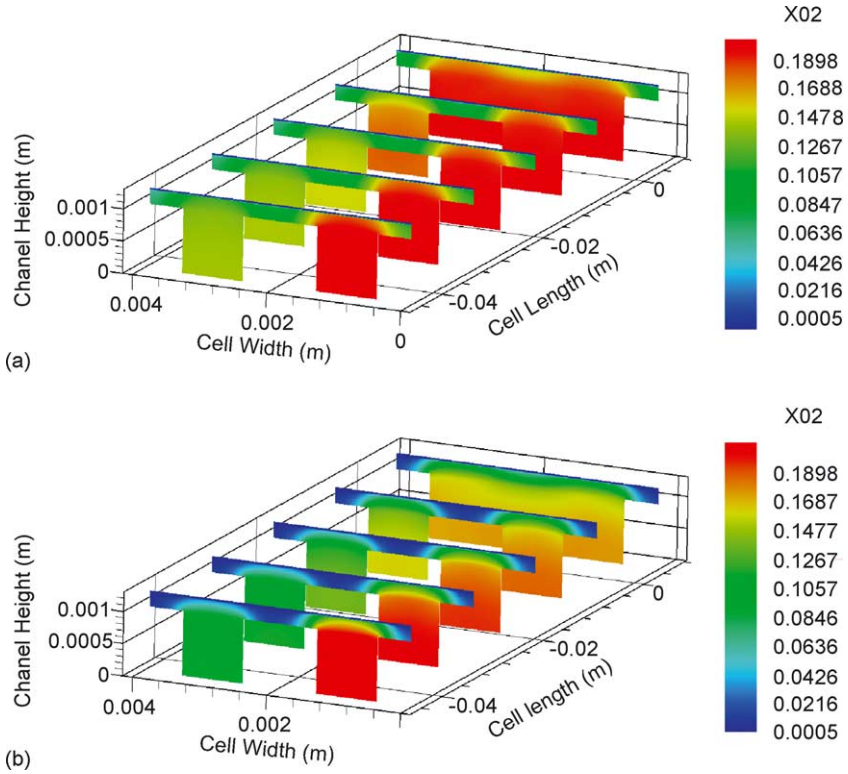

Fig. 4. Oxygen molar fraction distribution in the cathode side for two loading conditions: (a) 0.3 A cm^{-2} and (b) 1.2 A cm^{-2}.

is more pronounced for high load conditions, where oxygen under the land area is almost completely depleted.

The variation of the cathode activation overpotentials is shown in Fig. 5. For both loading conditions, the distribution patterns of activation overpotentials are similar, with higher values under the land area. This uneven distribution is due to lower ohmic losses under the land area than under the channel area. Since the activation overpotential has an exponential effect on the magnitude of local current, the conditions for generating current under the land area are more favorable in the absence of oxygen transport limitations. The enhanced capability for producing current under the land areas when oxygen transport is not limited is illustrated in Fig. 6 which shows distribution patterns that are quite different from those obtained in previous studies in which a constant overpotential is assumed. For the low load case illustrated, oxygen diffusion is not limiting, and the current density is higher under the land area. However, as loading increases, oxygen transport limitations under the land area become significant, resulting in the shift of higher current density towards the channel area where oxygen concentration is higher.

Ohmic overpotential is the loss associated with resistance to electron transport in the gas diffusion layers. For a given load, the magnitude of this overpotential is dependent on the path of the electrons. The longer the path, the larger the potential drop. Under the channel area the catalyst layer is farthest from the collector plate and locally 'edge' collection

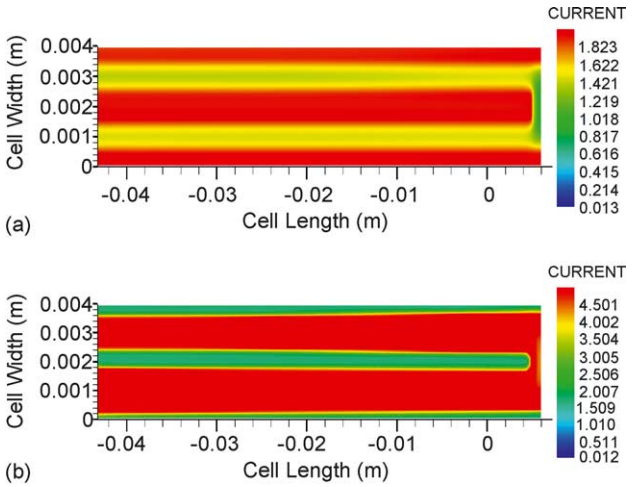

Fig. 6. Relative current density distribution in the first catalyst layer for two loading conditions: (a) 0.3 A cm^{-2} and (b) 1.2 A cm^{-2} (current densities normalized by 100 A cm^{-3}).

takes place, i.e. the current flows along a longer path along the width (*z*-direction) rather than across the GDL. Ohmic losses are thus higher than under the gas diffusion layer. Fig. 7 shows ohmic overpotential distribution patterns that are similar for both loading conditions. However, the magnitude of the potential loss increases with cell loading.

As indicated earlier, heat generation is only considered from the electrochemical reaction on the cathode side since

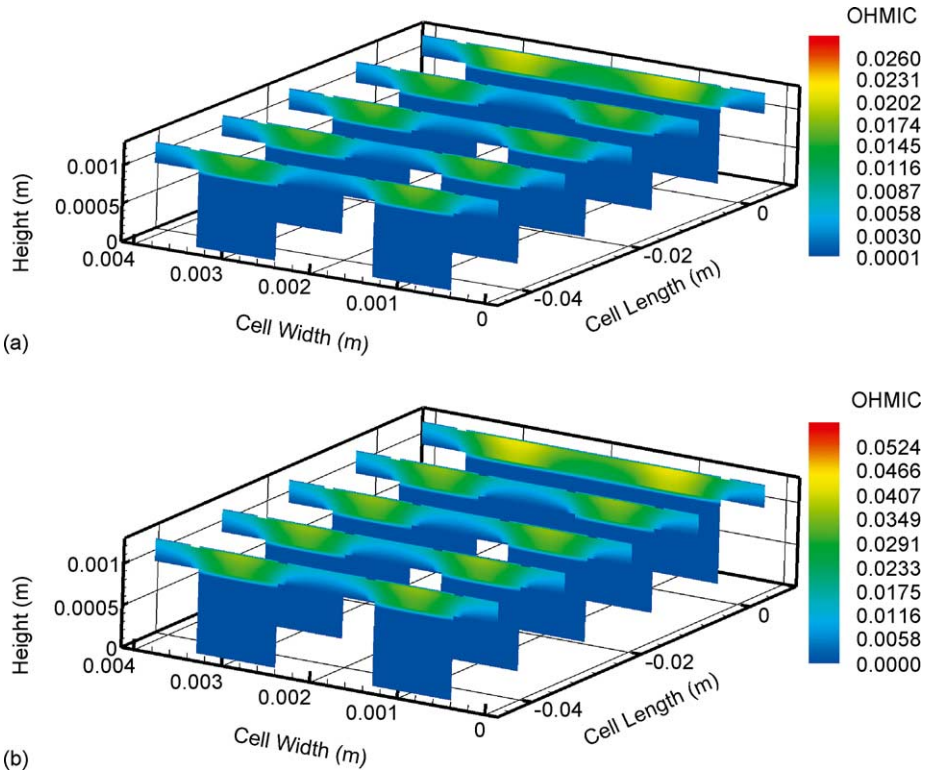

Fig. 7. Ohmic overpotential in the cathode gas diffusion layer and channel for two loading conditions: (a) 0.3 A cm^{-2} (b) 1.2 A cm^{-2}.

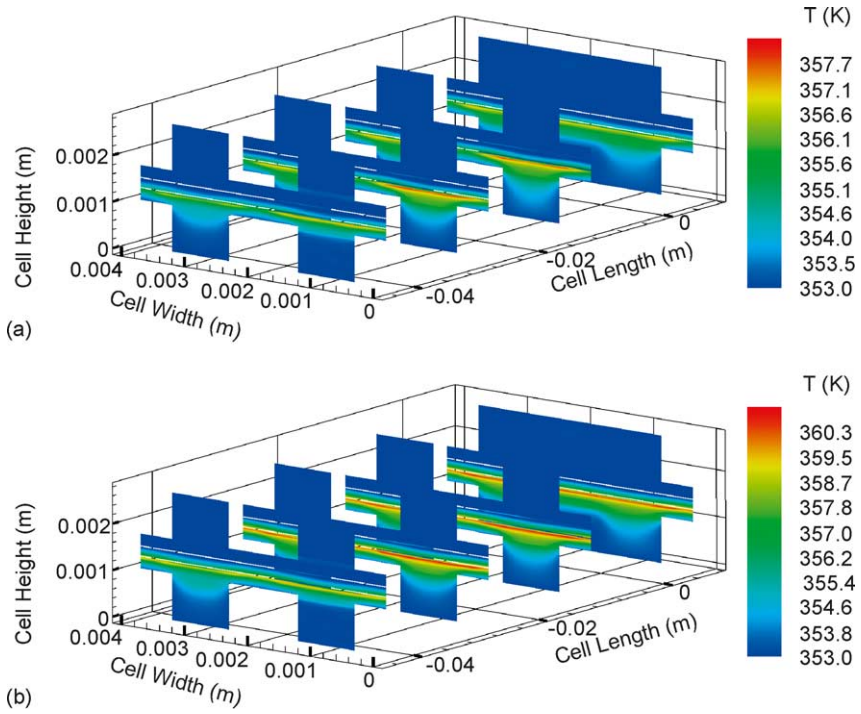

Fig. 8. Temperature distribution in the cell for two loading conditions: (a) 0.3 A cm^{-2} (b) 1.2 A cm^{-2}.

the activation is negligible in the anode side. The temperature distribution inside a fuel cell is highly dependent on the loading conditions and associated electrochemical activity. Temperature distributions for the intermediate and high load conditions are shown in Fig. 8. In both the cases, the highest temperatures are located at the cathode catalyst layer. Since the membrane conductivity is quite low and there is no heat generation on the anode side, the anode side temperature is quite uniform and equal to the anode gas stream temperature. On the other hand, the cathode gas temperature close to the channel gas diffusion layer interface is from 1 to 7 °C higher than the nominal operating temperature.

5. Conclusions

A three-dimensional computational fluid dynamics model of a PEM fuel cell with serpentine flow channels was developed. This model provides valuable information about the transport phenomena inside the fuel cell such as reactant gas concentration distribution, temperature distribution, potential distribution in the membrane and gas diffusion layers, activation overpotential distribution, and local current density distribution.

A unique feature of this model is the implementation of the voltage-to-current algorithm that allows for a more realistic spatial variation of the electrochemical kinetics. In addition, the three-dimensional activity of the catalyst layer is also accounted for in this model.

The computational procedure involves the coupling of the potential field with the reactant species concentration field. Rather than assuming a constant surface overpotential over the entire fuel cell, the spatial variation of the cathodic surface overpotential is computed locally, resulting in improved prediction of the local current density distribution. The current density distribution patterns are found to vary with loading conditions. At low load, the current density is higher under the land area. As the load is increased, the current density maxima shift towards the center of the channel. These local current density distribution patterns are radically different from those obtained with models that do not account for the non-uniformity of surface overpotential.

Acknowledgements

The authors wish to thank Prof. Hongtan Liu for supplying experimental data, and acknowledge stimulating discussions with Mads Bang the assistance of Shawn Litster with graphics. This work was supported by a Discovery grant from the Natural Sciences and Engineering Research Council of Canada.

References

[1] T.E. Springer, T.A. Zawodzinski, S. Gottesfeld, J. Electrochem. Soc. 138 (8) (1991) 2334–2342.
[2] D.M. Bernardi, M.W. Verbrugge, AIChE J. 37 (8) (1991) 1151–1162.
[3] T.V. Nguyen, R.E. White, J. Electrochem. Soc. 140 (8) (1993) 2178–2186.
[4] T.F. Fuller, J. Newman, J. Electrochem. Soc. 140 (5) (1993) 1218–1225.
[5] V. Gurau, H. Liu, S. Kakac, AIChE J. 44 (11) (1998) 2410–2421.

[6] T. Berning, D.M. Lu, N. Djilali, J. Power Sources 106 (2002) 284–294.
[7] Z.H. Wang, C.Y. Wang, K.S. Chen, J. Power Sources 94 (1) (2001) 40–50.
[8] D. Natarajan, T.V. Nguyen, J. Electrochem. Soc. 148 (12) (2001) 1324–1335.
[9] T. Berning, N. Djilali, J. Electrochem. Soc. 150 (12) (2003) A1598–A1607.
[10] M.J. Lampinen, M. Fomino, J. Electrochem. Soc. 140 (12) (1993) 3537–3546.
[11] R. Taylor, R. Krishna, Multicomponent Mass Transfer, Wiley, New York, 1993.
[12] R.E. De La Rue, C.W. Tobias, J. Electrochem. Soc. 106 (9) (1959).
[13] D.M. Bernadi, M.W. Verbrugge, J. Electrochem. Soc. 139 (9) (1992) 2477–2491.
[14] A. Parthasarathy, S. Srinivasan, A.J. Appleby, C.R. Martin, J. Electrochem. Soc. 139 (9) (1992) 2530–2537.
[15] L. Wang, A. Husar, T. Zhou, H. Liu, Int. J. Hydrogen Energy 28 (2003) 1263–1272.